



A Mechanism for Brightening

Linear Stability Analysis of the Curvature-Enhanced Coverage Model

G. B. McFadden,^z S. R. Coriell, T. P. Moffat,* D. Josell, D. Wheeler,
W. Schwarzscher,* and J. Mallett

National Institute of Standards and Technology, Gaithersburg, Maryland 20899-8910, USA

This work presents experiments and theory describing a mechanism for how brighteners in electrolytes function. The mechanism involves change of local coverage of a deposition rate-enhancing catalyst adsorbed on the surface through change of local surface area during growth as well as accumulation and consumption. A first-order perturbation analysis shows the surface is stable against growth of perturbations for all wavelengths below a critical value that is deposition-condition dependent. The model predictions are shown to be consistent with the experimental results.

© 2003 The Electrochemical Society. [DOI: 10.1149/1.1593042] All rights reserved.

Manuscript submitted September 18, 2002; revised manuscript received March 3, 2003. Available electronically July 24, 2003.

Roughness evolution during electrodeposition is a subject of wide-ranging scientific and technical interest. Experience has shown that metal ion depletion at the interface is usually associated with destabilization of planar growth fronts. This has been explained by Mullins-Sekerka morphological stability theory which examines system response to small perturbations from steady-state growth conditions. Typically, a sinusoidal variation of surface height is imposed on the flat surface, and the resulting time evolution, to first order in the amplitude of the perturbation, is analyzed.^{1,2} A positive growth rate reflects instability while a negative value results in attenuation of the perturbation; the former yields a rough surface while the latter case gives a smooth interface. This type of analysis has been widely applied to study phase transformations ranging from solidification,^{1,2} to additive-free electroplating,³⁻¹¹ and chemical vapor deposition.^{12,13} In contrast to the destabilizing influence of the reactant gradient, it is known that capillarity, adatom diffusion, and reaction kinetics dampen, and even stabilize the system, particularly at shorter wavelengths.

An important aspect of electroplating practice involves the use of electrolyte additives to generate smooth, optically bright films. In certain instances, additives even allow the leveling of undesired surface imperfections by inducing preferential deposition at the bottoms of features such as scratches. The traditional leveling mechanism behind this process is the existence of a concentration gradient of the inhibiting additive that results in lower deposition of the inhibitor, with associated decreasing inhibition of the metal deposition, the farther down one goes in the defect.¹⁴⁻¹⁷ It is generally known that electrolytes that otherwise deposit at equal rates on all surfaces can be induced to deposit preferentially at the bottoms of polishing scratches and other surface imperfections through the addition of deposition-rate inhibiting additives.

It is generally recognized that the traditional leveling mechanism will not affect deposition substantially when the dimensions of the defect are orders of magnitude smaller than the thickness of the boundary layer responsible for the concentration gradient. For optically relevant dimensions that are only a fraction of 1 μm and a typical boundary layer thickness of 100 μm , the appropriateness of such a model becomes questionable. For this reason, electrolytes commonly used for industrial plating applications that require optically bright deposits typically contain a variety of additives that have been empirically determined to yield bright deposits. There is no fundamental basis for determining which additives to add or why.

Recent publications have detailed a mechanism for the superconformal deposition process now used to achieve bottom-to-top filling of submicrometer dimension features. The mechanism involves (i) the adsorption of a deposition-rate enhancing catalyst on the deposit

surface and (ii) changes in the local catalyst coverage induced by the changing surface area on regions with nonzero curvature.^{18,19} Models based on this curvature enhanced accelerator coverage (CEAC) mechanism yield predictions of superconformal filling of fine features due to the increase of catalyst coverage during deposition on the concave bottom surfaces of filling features.¹⁸⁻²² The implications for brightening of a mechanism that increases deposition rates at the bottoms of valleys (concave surfaces) while slowing deposition on the tops of hills (convex surfaces) have been noted. This mechanism has also been shown to describe superconformal feature filling by surfactant catalyzed chemical vapor deposition (CVD) of copper.²³

This work presents a linear stability analysis to establish just how such a mechanism would stabilize a surface against roughening as well as determining the parameters and conditions for which such a mechanism will function optimally. An infinitesimal sinusoidal perturbation of the surface height and catalyst coverage is imposed on the flat surface, and the resulting time evolution to the first order in the amplitude of the perturbation is analyzed. In the tradition of morphological stability analyses, the real part of the complex exponent that describes the time dependence of the perturbation amplitude determines the stability of the surface. A positive value indicates growth of the instability while a negative value results in attenuation.

Governing Equations

We consider electrodeposition of copper from an aqueous solution containing copper ions of concentration C_c and a catalyst (accelerator) of concentration C_a in the presence of an overvoltage η . We assume that growth of solid copper occurs at constant velocity V in the z direction. Diffusion equations in the solution for C_c and the catalyst C_a are written in a reference frame moving with this constant velocity

$$\frac{\partial C_c}{\partial t} - V \frac{\partial C_c}{\partial z} = D_c \nabla^2 C_c \quad [1]$$

$$\frac{\partial C_a}{\partial t} - V \frac{\partial C_a}{\partial z} = D_a \nabla^2 C_a \quad [2]$$

where t is time, and the constants D_c and D_a are the diffusion coefficients for C_c and C_a , respectively. The mean position of the liquid-solid interface is assumed to be $z = 0$. Far-field boundary conditions in the solution are applied at the edge of a boundary layer at $z = \delta$

$$C_c = C_c^\infty \quad C_a = C_a^\infty \quad [3]$$

The catalyst is adsorbed on the solid-liquid interface and has a saturation coverage Γ_0 . The fractional catalyst coverage is described by

* Electrochemical Society Active Member.

^z E-mail: mcfadden@nist.gov

a dimensionless parameter θ , defined so that $\Gamma_0\theta$ is the local interface coverage in units of moles per unit area. The coverage is governed by

$$\frac{d\theta}{dt} = k^+(1 - \theta)C_a - k^-\theta^n + v_N\mathcal{K}\theta \quad [4]$$

where $v_N = (V + h_t)/\sqrt{1 + h_x^2}$ is the normal velocity of the interface $z = h(x, t)$, $\mathcal{K} = h_{xx}/[1 + h_x^2]^{3/2}$ is the mean curvature of the interface, and the exponent n is a constant. Here we have assumed a two-dimensional interface for notational simplicity, but the results can be immediately applied to a general three-dimensional interface. Our sign convention is such that the curvature of a solid sphere is negative. The parameters k^+ and k^- describe the adsorption and desorption of the catalyst at the interface and depend on the over-voltage η . We use the specific forms

$$k^+ = 230 \exp(-f\eta/2) \quad [\text{cm}^3/\text{mol s}] \quad [5]$$

$$k^- = -0.08\eta$$

$$+ \frac{1.1}{\exp(-35[\eta + 0.098]) + \exp(45[\eta + 0.098])} [\text{s}^{-1}] \quad [6]$$

where $f = \mathcal{F}/RT$, \mathcal{F} is Faraday's constant, R is the ideal gas constant, and T is the temperature; here η is measured in volts. The values used approximate the kinetics for an electrolyte that is described later. The particular forms of the voltage dependence have no bearing on the nature of the stabilization problem beyond the values of k^+ and k^- that they yield.

Flux conditions at the interface are given by

$$D_c \frac{\partial C_c}{\partial \mathbf{N}} = -v_N(C_c - V_c) \quad [7]$$

$$D_a \frac{\partial C_a}{\partial \mathbf{N}} = \Gamma_0 k^+(1 - \theta)C_a \quad [8]$$

where $V_c = 1/\Omega$, Ω is the molar volume of solid copper, and \mathbf{N} is the normal vector to the interface. In writing Eq. 8 we have neglected a term of the form $v_N C_a$ that is expected to be small compared to the other terms. We have also assumed that there is no desorption of the strongly adsorbing catalyst from the surface of the solid; rather the $k^-\theta^n$ loss term in Eq. 4 represents either incorporation (trapping) of catalyst within the solid, where it has no effect on deposition, and/or desorption of an inactivated part of the catalyst molecule.

The normal velocity satisfies the relation

$$v_N = \frac{i\Omega}{2\mathcal{F}} \quad [9]$$

where the current i is given by the Butler-Volmer equation

$$i = i_0(\theta) \frac{C_c}{C_c^\infty} \exp\left\{-\alpha(\theta) \left[\frac{\mathcal{F}\eta - \Omega\gamma\mathcal{K}}{RT} \right]\right\} \quad [10]$$

we have neglected the current due to the reverse reaction. Here γ is the free energy of the solid-liquid interface. We use a model with

$$i_0(\theta) = b_0 + b_1\theta \quad [11]$$

$$\alpha(\theta) = m_0 + m_1\theta \quad [12]$$

values for the constants b_0 , b_1 , m_0 , and m_1 that we use are also given in Table I.

Table I. Thermophysical properties used in calculations.

Bulk concentration of cupric ion	C_c^∞	2.78×10^{-4}	mol/cm ³
Diffusion coefficient for catalyst	D_a	5.6×10^{-6}	cm ² /s
Diffusion coefficient for cupric ion	D_c	5.6×10^{-6}	cm ² /s
Faraday constant	\mathcal{F}	96,485	C/mol
Ideal gas constant	R	8.314	J/K mol
Temperature	T	298	K
Surface energy	γ	1.952×10^{-4}	J/cm ²
Saturation surface coverage	Γ_0	0.635×10^{-9}	mol/cm ²
Thickness of hydrodynamic boundary layer	δ	0.0156	cm
Molar volume of copper	Ω	7.1	cm ³ /mol
Exchange current density	b_0	0.026×10^{-3}	A/cm ²
coverage dependence	b_1	4.5×10^{-3}	A/cm ²
Metal deposition transfer coefficient	m_0	0.5	
coverage dependence	m_1	0.0	
Coverage exponent	n	3	

Base State

The stability of the system is considered by perturbing an initially planar interface and determining whether the perturbations grow or decay in time. The perturbed quantities, assumed to be small, are denoted by a superscript (1) and the unperturbed base state is denoted by a superscript (0).

The base state satisfies

$$k^+(1 - \theta^{(0)})C_a^I - k^-[\theta^{(0)}]^n = 0 \quad [13]$$

$$C_c^{(0)}(z) = C_c^I + (C_c^\infty - C_c^I) \frac{[1 - \exp(-zV/D_c)]}{[1 - \exp(-\delta V/D_c)]} \quad [14]$$

$$C_a^{(0)}(z) = C_a^I + (C_a^\infty - C_a^I) \frac{[1 - \exp(-zV/D_a)]}{[1 - \exp(-\delta V/D_a)]} \quad [15]$$

where $C_c^I = C_c^{(0)}(z=0)$ and $C_a^I = C_a^{(0)}(z=0)$ denote the concentrations at the planar interface. We denote the unperturbed solute gradients at the planar interface by

$$G_c = \frac{dC_c^{(0)}}{dz}(z=0) = \frac{-V(C_c^I - V_c)}{D_c} \quad [16]$$

$$G_a = \frac{dC_a^{(0)}}{dz}(z=0) = \frac{\Gamma_0 k^+(1 - \theta^{(0)})C_a^I}{D_a} \quad [17]$$

By substituting the concentration fields given by Eq. 14 and 15 into the flux conditions in Eq. 7 and 8 we obtain

$$C_c^I = V_c + (C_c^\infty - V_c)\exp(\delta V/D_c) \quad [18]$$

$$C_a^I = \frac{VC_a^\infty}{V + \Gamma_0 k^+(1 - \theta^{(0)})[1 - \exp(-\delta V/D_a)]} \quad [19]$$

The unperturbed interface velocity is given by

$$V = \frac{i_0(\theta^{(0)})\Omega C_c^I}{2\mathcal{F}C_c^\infty} \exp\left[\frac{-\alpha(\theta^{(0)})\mathcal{F}\eta}{RT} \right] \quad [20]$$

We note that for $\delta V/D_c \ll 1$ and $\delta V/D_a \ll 1$, we may approximate the exponentials in Eq. 19 and 18 to obtain

$$C_a^I = \frac{C_a^\infty}{1 + \Gamma_0 k^+(1 - \theta^{(0)})\delta/D_a} \quad [21]$$

and

$$C_c^I = C_c^\infty + (C_c^\infty - v_c)\delta/D_c \quad [22]$$

The four unknowns C_a^1 , C_c^1 , V , and $\theta^{(0)}$ are determined by Eq. 13, 18, 19 and 20. These nonlinear equations are solved numerically to determine the base state.

Perturbed System

We perturb the system by writing

$$\begin{pmatrix} C_c(x,z,t) \\ C_a(x,z,t) \\ \theta(x,t) \\ h(x,t) \end{pmatrix} = \begin{pmatrix} C_c^{(0)}(z) \\ C_a^{(0)}(z) \\ \theta^{(0)} \\ 0 \end{pmatrix} + \exp(\sigma t + i\omega x) \begin{pmatrix} C_c^{(1)}(z) \\ C_a^{(1)}(z) \\ \hat{\theta} \\ \hat{h} \end{pmatrix} + \dots \quad [23]$$

where σ is the temporal growth rate of the perturbation amplitudes and ω is the wavenumber of the sinusoidal interface perturbation. The wavelength of the perturbation is given by $\lambda = 2\pi/\omega$.

The perturbed concentration fields are given by

$$C_j^{(1)}(z) = \hat{C}_j \frac{\exp(-Vz/2D_j)[\exp(-R_j z) - \exp(R_j z)\exp(-2R_j \delta)]}{1 - \exp(-2R_j \delta)} \quad [24]$$

for $j = c$ and $j = a$, with

$$R_j = \sqrt{\left(\frac{V}{2D_j}\right)^2 + \frac{\sigma}{D_j} + \omega^2} \quad [25]$$

The perturbed flux conditions are obtained by linearizing the boundary conditions given by Eq. 7 and 8 and inserting the perturbed concentration fields given from Eq. 24. The linearized boundary conditions are applied at $z = 0$, and are obtained by taking into account the variations associated with both the perturbed concentration fields and the perturbed interface height. Specifically, a general function $f(x,z,t) = f^{(0)}(z) + f^{(1)}(x,z,t) + \dots$ evaluated at the perturbed interface position $z = h^{(1)}(x,t)$ has the expansion

$$\begin{aligned} f[x, h^{(1)}(x,t), t] &\approx f^{(0)}[h^{(1)}(x,t)] + f^{(1)}[x, h^{(1)}(x,t), t] + \dots \\ &\approx f^{(0)}(0) + \left\{ f^{(1)}(x,0,t) + \frac{df^{(0)}}{dz}(0)h^{(1)}(x,t) \right\} \\ &+ \dots \end{aligned} \quad [26]$$

through first order in the perturbation amplitudes. This type of expansion applies to the interface concentrations and also to their normal derivatives, since to first order the normal derivative is equal to the derivative with respect to z . For the boundary conditions given by Eq. 7 and 8 this procedure results in the expressions

$$\begin{aligned} -D_c \frac{[(R_c + V/2D_c) + (R_c - V/2D_c)\exp(-2R_c \delta)]}{[1 - \exp(-2R_c \delta)]} \hat{C}_c \\ = -\sigma \hat{h} [C_c^1 - V_c] - V \hat{C}_c \end{aligned} \quad [27]$$

and

$$\begin{aligned} B_a \hat{C}_a + D_a \frac{d^2 C_a^{(0)}}{dz^2}(z=0) \hat{h} = -\Gamma_0 k^+ C_a^1 \hat{\theta} + \Gamma_0 k^+(1 - \theta^{(0)}) \\ \times [\hat{C}_a + G_a \hat{h}] \end{aligned} \quad [28]$$

where

$$B_a = -D_a \frac{[(R_a + V/2D_a) + (R_a - V/2D_a)\exp(-2R_a \delta)]}{[1 - \exp(-2R_a \delta)]} \quad [29]$$

Linearizing the Butler-Volmer equation gives

$$\begin{aligned} \left(\frac{\sigma}{V}\right) \hat{h} = \left[\frac{i_0'(\theta^{(0)})}{i_0(\theta^{(0)})} - \frac{\mathcal{F}\eta}{RT} \alpha'(\theta^{(0)}) \right] \hat{\theta} + \left[\frac{G_c}{C_c^1} - \frac{\alpha(\theta^{(0)})\Omega\gamma\omega^2}{RT} \right] \hat{h} \\ + \frac{1}{C_c^1} \hat{C}_c \end{aligned} \quad [30]$$

The linearized coverage equation is

$$\begin{aligned} \sigma \hat{\theta} = k^+(1 - \theta^{(0)})[\hat{C}_a + G_a \hat{h}] - k^+ C_a^1 \hat{\theta} - n[\theta^{(0)}]^{n-1} k^- \hat{\theta} \\ - V\theta^{(0)}\omega^2 \hat{h} \end{aligned} \quad [31]$$

Dispersion Relation

To derive the dispersion relation, we first eliminate \hat{C}_c from Eq. 27 to obtain

$$\hat{C}_c = \sigma A \hat{h} \quad [32]$$

where

$$A = \frac{[1 - \exp(-2R_c \delta)]G_c/V}{[(V/2D_c - R_c) - (V/2D_c + R_c)\exp(-2R_c \delta)]} \quad [33]$$

Next, using $C_a^{(0)}(z)$ from Eq. 15 and the definition of G_a from Eq. 17, Eq. 28 gives

$$\begin{aligned} 0 = [\Gamma_0 k^+(1 - \theta^{(0)}) - B_a] \hat{C}_a + G_a [\Gamma_0 k^+(1 - \theta^{(0)}) + V] \hat{h} \\ - \Gamma_0 k^+ C_a^1 \hat{\theta} \end{aligned} \quad [34]$$

Then, from Eq. 30 and 32 we have

$$0 = VF \hat{\theta} + \left[\frac{VG_c}{C_c^1} - \frac{\alpha(\theta^{(0)})\Omega V\gamma\omega^2}{RT} + \frac{V\sigma A}{C_c^1} - \sigma \right] \hat{h} \quad [35]$$

where

$$F = \frac{i_0'(\theta^{(0)})}{i_0(\theta^{(0)})} - \frac{\mathcal{F}\eta}{RT} \alpha'(\theta^{(0)}) \quad [36]$$

Finally, Eq. 31 can be rewritten

$$\begin{aligned} 0 = [k^+(1 - \theta^{(0)})] \hat{C}_a - [\sigma + k^+ C_a^1 + n[\theta^{(0)}]^{n-1} k^-] \hat{\theta} \\ + [G_a k^+(1 - \theta^{(0)}) - V\theta^{(0)}\omega^2] \hat{h} \end{aligned} \quad [37]$$

Equations 32, 34, 35, and 37 constitute four homogeneous linear equations in the variables \hat{C}_c , \hat{C}_a , \hat{h} , and $\hat{\theta}$. Setting the determinant of the linear system to zero provides a dispersion relation of the form

$$\begin{aligned}
& -B_a \left\{ VF[G_a k^+(1 - \theta^{(0)}) - V\theta^{(0)}\omega^2] + (\sigma + k^+ C_a^I \right. \\
& \quad + n[\theta^{(0)}]^{n-1} k^-) \left(\frac{VG_c}{C_c^I} - \frac{\alpha[\theta^{(0)}]\Omega V\gamma\omega^2}{RT} \right. \\
& \quad \left. \left. + \frac{V\sigma A}{C_c^I} - \sigma \right) \right\} + k^+(1 - \theta^{(0)}) \left\{ \Gamma_0(\sigma + n[\theta^{(0)}]^{n-1} k^-) \right. \\
& \quad \times \left(\frac{VG_c}{C_c^I} - \frac{\alpha(\theta^{(0)})\Omega V\gamma\omega^2}{RT} + \frac{V\sigma A}{C_c^I} - \sigma \right) \\
& \quad \left. - \Gamma_0 V^2 F \theta^{(0)} \omega^2 - V^2 F G_a \right\} \\
& = 0 \tag{38}
\end{aligned}$$

Approximate Solution for Large ω

If we assume that ω is large enough that the square of the wave-number dominates both $(V/2D_j)^2$ and $|\sigma|/D_j$ then $R_j \approx \omega$. If we further assume that $\delta\omega \gg 1$, then $B_a \approx -D_a\omega$ and $A \approx -G_c/(V\omega)$. Thus the term proportional to B_a dominates the dispersion relation Eq. 38, and neglecting A gives the approximate dispersion relation

$$\begin{aligned}
& VF[G_a k^+(1 - \theta^{(0)}) - V\theta^{(0)}\omega^2] + (\sigma + k^+ C_a^I + n[\theta^{(0)}]^{n-1} k^-) \\
& \quad \times \left(\frac{VG_c}{C_c^I} - \frac{\alpha(\theta^{(0)})\Omega V\gamma\omega^2}{RT} - \sigma \right) = 0 \tag{39}
\end{aligned}$$

or

$$\begin{aligned}
& \sigma^2 + \left[k^+ C_a^I + n[\theta^{(0)}]^{n-1} k^- - \frac{VG_c}{C_c^I} + \frac{\alpha(\theta^{(0)})\Omega V\gamma\omega^2}{RT} \right] \sigma \\
& \quad - VF[G_a k^+(1 - \theta^{(0)}) - V\theta^{(0)}\omega^2] - [k^+ C_a^I \\
& \quad + n[\theta^{(0)}]^{n-1} k^-] \left(\frac{VG_c}{C_c^I} - \frac{\alpha(\theta^{(0)})\Omega V\gamma\omega^2}{RT} \right) = 0 \tag{40}
\end{aligned}$$

We note that in the exact dispersion relation Eq. 38, A only appears as the product σA . At an onset of instability with $\sigma = 0$ (real mode), A therefore has no effect on the critical wavenumber. We find that the complex modes with $\sigma_i \neq 0$ have large critical wavenumbers, so that A is negligible for these modes as well.

Equation 40 is the same dispersion relation that is obtained by linearizing the system

$$\frac{d\theta}{dt} = k^+(1 - \theta)C_a - k^-\theta^n + v_n \mathcal{K}\theta \tag{41}$$

$$v_n = i_0(\theta) \frac{\Omega C_c}{2\mathcal{F}C_c^\infty} \exp\left\{-\alpha(\theta)\left[\frac{\mathcal{F}\eta - \Omega\gamma\mathcal{K}}{RT}\right]\right\} \tag{42}$$

both evaluated at the interface, with the concentration fields given by

$$C_c(z) = C_c^I + G_c z \tag{43}$$

$$C_a(z) = C_a^I + G_a z \tag{44}$$

The values of C_c^I and C_a^I depend on δ and are obtained from the full expressions in Eq. 18 and 19. In other words, the linearized system obtained from Eq. 41 and 42

$$\begin{aligned}
& \sigma \hat{\theta} = k^+[1 - \theta^{(0)}]G_a \hat{h} - (k^+ C_a^I + n[\theta^{(0)}]^{n-1} k^-) \hat{\theta} \\
& \quad - V\theta^{(0)}\omega^2 \hat{h} \tag{45}
\end{aligned}$$

$$\sigma \hat{h} = \left[\frac{VG_c}{C_c^I} - \frac{\alpha(\theta^{(0)})\Omega V\gamma\omega^2}{RT} \right] \hat{h} + VF\hat{\theta} \tag{46}$$

also has the dispersion relation given by Eq. 40. Essentially, these small wavelength perturbations only sample, without affecting, the gradients in the concentration fields immediately adjacent to the interface.

If we ignore the coupling between $\hat{\theta}$ and \hat{h} in Eq. 45 by neglecting the terms proportional to \hat{h} , this equation represents a stable real mode with $\sigma = -(k^+ C_a^I + n[\theta^{(0)}]^{n-1} k^-)$. Similarly, if we neglect the term proportional to $\hat{\theta}$ in Eq. 46, this equation represents a real mode with $\sigma = VG_c/C_c^I - \alpha(\theta^{(0)})\Omega V\gamma\omega^2/RT$. The concentration gradient G_c is destabilizing, and the surface tension γ is stabilizing; the mode is unstable for small ω and stable for large ω . With the coupling included in these equations the situation is more complicated and, still assuming the modes are real, depends on the relative phase between $\hat{\theta}$ and \hat{h} . For example, if they are in phase, with $\hat{\theta}/\hat{h} > 0$, the positive term VF in Eq. 46 is destabilizing and is stabilizing if they are out of phase, with $\hat{\theta}/\hat{h} < 0$. For Eq. 45, the coupling depends on the sign of the term $k^+[1 - \theta^{(0)}]G_a - V\theta^{(0)}\omega^2$, which is positive for small ω and negative for large ω .

When this term is negative, the mode is stabilized if $\hat{\theta}$ and \hat{h} are in phase, and destabilized if they are out of phase. The relative phase of $\hat{\theta}$ and \hat{h} are determined by examining the linearized boundary conditions once σ has been determined. In many cases, at the onset of instability they are found to be out of phase. In the limit of large wavenumbers, the perturbed interfacial concentrations \hat{C}_c and \hat{C}_a both vanish to leading order. More generally, at the onset of instability for a real mode ($\sigma = 0$) Eq. 32 shows that the relative phase between \hat{C}_c and \hat{h} changes from being in phase to being out of phase as the growth rate passes through zero.

The solution to the approximate dispersion relation in Eq. 40 can be written in the form

$$\begin{aligned}
& \sigma = \frac{1}{2} \left(\frac{VG_c}{C_c^I} - \frac{\alpha(\theta^{(0)})\Omega V\gamma\omega^2}{RT} - k^+ C_a^I - n[\theta^{(0)}]^{n-1} k^- \right) \\
& \quad \pm \sqrt{\frac{1}{4} \left(\frac{VG_c}{C_c^I} - \frac{\alpha(\theta^{(0)})\Omega V\gamma\omega^2}{RT} + k^+ C_a^I + n[\theta^{(0)}]^{n-1} k^- \right)^2 + VFG_a k^+(1 - \theta^{(0)}) - V^2 F \theta^{(0)} \omega^2} \tag{47}
\end{aligned}$$

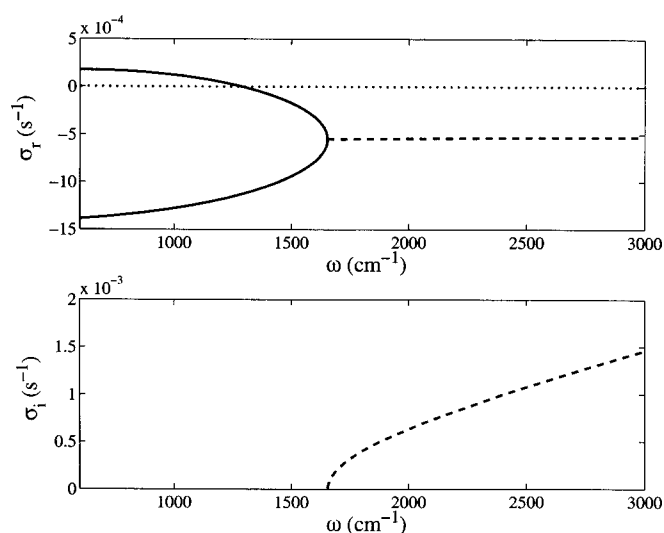


Figure 1. The real and imaginary parts of the temporal growth rate σ as a function of the wavenumber ω of a sinusoidal perturbation for $\eta = -0.3$ V and $C_a^\infty = 1.0 \times 10^{-9}$ mol/cm³. The axis $\sigma_r = 0$ is indicated by the dotted line.

The stability criterion for a quadratic of the form

$$\sigma^2 + a_1\sigma + a_2 = 0 \quad [48]$$

(See Ref. 24)

$$a_1 \geq 0 \quad a_2 \geq 0 \quad [49]$$

if either of these conditions is violated the solution is unstable. For our system, the condition $a_1 > 0$ yields

$$\left[\frac{\alpha(\theta^{(0)})\Omega V\gamma}{RT} \right] \omega^2 \geq \frac{VG_c}{C_c^I} - k^+C_a^I - n[\theta^{(0)}]^{n-1}k^- \quad [50]$$

while the condition $a_2 > 0$ yields

$$\begin{aligned} & \left[VF\theta^{(0)} + \left(\frac{\alpha(\theta^{(0)})\Omega V\gamma}{RT} \right) (k^+C_a^I + n[\theta^{(0)}]^{n-1}k^-) \right] \omega^2 \\ & \geq F[G_a k^+(1 - \theta^{(0)})] + \left[\frac{G_c}{C_c^I} \right] (k^+C_a^I + n[\theta^{(0)}]^{n-1}k^-) \end{aligned} \quad [51]$$

The surface tension term in Eq. 50 guarantees that this inequality is satisfied for sufficiently large ω . For sufficiently large values of C_a^I the right side of Eq. 50 is negative, and stability is then determined by Eq. 51. In Eq. 51, the term $(G_c/C_c^I)(k^+C_a^I$

+ $n[\theta^{(0)}]^{n-1}k^-$) usually dominates the right side. On the left side, the term $VF\theta^{(0)}$ usually dominates the second term, proportional to $\alpha(\theta^{(0)})\Omega V\gamma/RT$, and hence the effects of surface tension are negligible. We next consider this limit.

Zero surface free energy limit ($\gamma=0$).—We first consider the simplified case in which we neglect the effects of surface-free energy. In that case, for large ω , such that

$$\begin{aligned} V^2F\theta^{(0)}\omega^2 & > \frac{1}{4} \left(\frac{VG_c}{C_c^I} + k^+C_a^I + n[\theta^{(0)}]^{n-1}k^- \right)^2 \\ & + VFG_a k^+(1 - \theta^{(0)}) \end{aligned} \quad [52]$$

a purely imaginary value is obtained for the radical in Eq. 47. Stability is therefore determined only by the sign of the term outside the radical, *i.e.*,

$$Re[\sigma] = \frac{1}{2} \left(\frac{VG_c}{2C_c^I} - k^+C_a^I - n[\theta^{(0)}]^{n-1}k^- \right) \quad [53]$$

We therefore have stability if

$$k^+C_a^I + n[\theta^{(0)}]^{n-1}k^- > \frac{VG_c}{C_c^I} \quad [54]$$

On the other extreme, for small ω , we have

$$\begin{aligned} & \frac{1}{4} \left(\frac{VG_c}{C_c^I} + k^+C_a^I + n[\theta^{(0)}]^{n-1}k^- \right)^2 \\ & - V^2F\theta^{(0)}\omega^2 > 0 \end{aligned} \quad [55]$$

so that a real value is obtained for the radical in Eq. 47, resulting in two real roots. In addition, since

$$VFG_a k^+(1 - \theta^{(0)}) + \frac{VG_c}{C_c^I} (k^+C_a^I + n[\theta^{(0)}]^{n-1}k^-) > 0 \quad [56]$$

the radical is the dominant term in Eq. 47, and there is one stable and one unstable root for small enough ω . (But we emphasize that this discussion applies to the approximate dispersion relation which was obtained in a large ω limit.) If Eq. 54 holds, the unstable root is stabilized for increasing ω by the term $V^2F\theta^{(0)}\omega^2$, and is neutrally stable at the marginal wavenumber given by

$$V^2F\theta^{(0)}\omega^2 = F[G_a k^+(1 - \theta^{(0)})] + \frac{G_c}{C_c^I} (k^+C_a^I + n[\theta^{(0)}]^{n-1}k^-) \quad [57]$$

When ω further increases to the value

Table II. Numerical results for $C_c^\infty = 2.78 \times 10^{-4}$ mol/cm³ and $\eta = -0.3$ V.

C_a^∞ (mol/cm ³)	C_a^I (mol/cm ³)	$10^5 C_c^I$ (mol/cm ³)	$\theta^{(0)}$	$10^7 V$ (cm/s)	ω_c (cm ⁻¹)	σ_i (s ⁻¹)
1.0×10^{-7}	9.37×10^{-8}	0.640	0.522	6.93	10452	0
1.0×10^{-8}	9.08×10^{-9}	1.178	0.275	6.79	3730.3	0
1.0×10^{-9}	8.92×10^{-10}	2.260	0.135	6.52	1289.9	0
1.0×10^{-10}	8.84×10^{-11}	4.205	0.0641	6.02	453.87	0
1.0×10^{-11}	8.80×10^{-12}	7.168	0.0300	5.27	13810	6.61×10^{-3}
1.0×10^{-12}	8.79×10^{-13}	10.73	0.0140	4.36	15579	5.69×10^{-3}
1.0×10^{-13}	8.78×10^{-14}	13.99	0.00652	3.53	13931	3.57×10^{-3}
1.0×10^{-14}	8.78×10^{-15}	16.28	0.00303	2.94	12402	2.13×10^{-3}

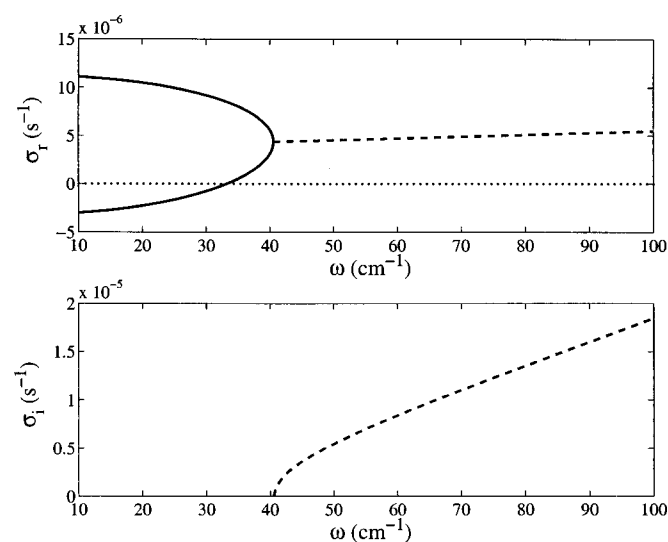


Figure 2. The real and imaginary parts of the temporal growth rate σ as a function of the wavenumber ω of a sinusoidal perturbation for $\eta = -0.3$ V and $C_a^\infty = 1.0 \times 10^{-13}$ mol/cm³. The axis $\sigma_r = 0$ is indicated by the dotted line.

$$V^2 F \theta^{(0)} \omega^2 = \frac{1}{4} \left(\frac{V G_c}{C_c^I} + k^+ C_a^I + n [\theta^{(0)}]^{n-1} k^- \right)^2 + V F G_a k^+ [1 - \theta^{(0)}] \quad [58]$$

the two real modes coincide, and for larger ω we obtain a pair of stable complex conjugate modes.

The limit of vanishing catalyst concentration.—If there is no catalyst present in the electrolyte, $C_a^\infty = 0$, then the coverage $\theta^{(0)}$ also vanishes and the dispersion Relation 47 reduces to

$$\frac{\sigma}{V} = \frac{G_c}{C_c^I} - \frac{m_0 \Omega \gamma \omega^2}{RT} \quad [59]$$

Because the copper concentration in the solid is much higher than that in the liquid, $V_c \gg C_c^I$, Eq. 16 and 20 yield

$$\frac{G_c}{C_c^I} \approx \frac{b_0}{2D_c \mathcal{F} C_c^\infty} \exp\left\{ \frac{-m_0 \mathcal{F} \eta}{RT} \right\} \quad [60]$$

Since $G_c/C_c^I > 0$, the interface is unstable for small ω and is stabilized by surface tension for sufficiently large ω . For the values listed in Table I, we have $m_0 \Omega \gamma / RT = 2.80 \times 10^{-7}$ cm. For $\eta = -0.3$ V we then find that the system is stable for $\omega > 1.0 \times 10^4$ cm⁻¹. It is important to note that the kinetics used through-

out this paper are for base electrolytes containing inhibiting polyethylene glycol (PEG) and chloride ions (Cl⁻), (concentrations given later) in addition to the catalyst; thus, in the limit of vanishing catalyst concentration, the kinetics modeled are those for the fully inhibited PEG-Cl-containing electrolyte.

Numerical Results

We have carried out numerical calculations for the parameter values given in Table I for various values of the bulk catalyst concentration C_a^∞ and the overpotential η . The numerical calculations were performed using the full dispersion relation given in Eq. 38, however, we also find that the approximate dispersion relation given by Eq. 40 is an excellent approximation, except at very small values of ω (*i.e.*, at longer wavelengths λ). We note that for very small values of ω we have found additional stable modes that play no role in the consideration of the stability of the system.

In Fig. 1 we show the real and imaginary parts of the temporal growth rate, σ_r and σ_i , as functions of the wavenumber ω for $\eta = -0.3$ V and $C_a^\infty = 1.0 \times 10^{-9}$ mol/cm³. The associated steady-state surface coverage of catalyst and cupric ion concentration near the interface can be found in Table II. The system is stable ($\sigma_r < 0$) for wavenumbers greater than ω_c , where the critical wavenumber ω_c denotes the largest value of ω for which $\sigma_r = 0$. In Fig. 1, $\omega_c = 1289.9$ cm⁻¹ ($\lambda_c = 49$ μ m). The solid curves correspond to real modes ($\sigma_i = 0$), for which the temporal growth rate of the perturbation is monotonic (nonoscillatory) in time. The dashed curve in Fig. 1 corresponds to a complex mode with $\sigma_i \neq 0$, in which case the growth rate is oscillatory in time. For small ω , one of the real modes is stable and the other unstable. The unstable mode becomes stable at the critical wavenumber ω_c . At ω_c the values of $\hat{\theta}$ and \hat{h} are 180° out of phase for both of the modes; that is, $\hat{\theta}/\hat{h}$ is real and negative. Thus the catalyst coverage and the deposition rate are enhanced in troughs and depressed on peaks, consistent with stabilization of the interface. At larger values of ω the two real modes merge into a complex mode with complex conjugate growth rates $\sigma_r \pm i\sigma_i$. The complex mode, with its negative σ_r , is stable for all wavenumbers. As ω increases further, σ_i steadily increases while σ_r decreases slightly; for example, for $\omega = 63052$ cm⁻¹ ($\lambda = 1.004$ μ m) we have $\sigma_r = -8.4 \times 10^{-4}$ s⁻¹ and $\sigma_i = \pm 0.04$ s⁻¹.

In Fig. 2 we show σ_r and σ_i as functions of the wavenumber ω for $\eta = -0.3$ V and $C_a^\infty = 1.0 \times 10^{-13}$ mol/cm³. There are again two real modes for small ω . However, both the real modes and the complex branch into which they merge are unstable ($\sigma_r \approx 5 \times 10^{-6}$ s⁻¹) for $\omega \approx 36$ cm⁻¹. For larger values of ω , σ_r increases to a maximum of about 10^{-5} s⁻¹ for $\omega \approx 2000$ cm⁻¹, and then decreases steadily, with $\sigma_r = 0$ for $\omega_c = 13931.0$ cm⁻¹ ($\lambda_c = 4.5$ μ m), with stability for $\omega > \omega_c$ due to capillarity (not shown). For $\omega = 62355$ cm⁻¹ ($\lambda = 0.99$ μ m), the growth rate has further decreased to $\sigma_r = -1.82 \times 10^{-4}$ s⁻¹.

Tables II and III summarize the numerical results for different catalyst concentrations C_a^∞ at $\eta = -0.3$ V and $\eta = -0.2$ V, re-

Table III. Numerical results for $C_c^\infty = 2.78 \times 10^{-4}$ mol/cm³ and $\eta = -0.2$ V.

C_a^∞ (mol/cm ³)	C_a^I (mol/cm ³)	$10^5 C_c^I$ (mol/cm ³)	$\theta^{(0)}$	$10^7 V$ (cm/s)	ω_c (cm ⁻¹)	σ_i (s ⁻¹)
1.0×10^{-7}	9.85×10^{-8}	6.87	0.260	5.34	1989.2	0
1.0×10^{-8}	9.83×10^{-9}	11.01	0.127	4.29	756.7	0
1.0×10^{-9}	9.82×10^{-10}	15.80	0.0605	3.06	304.2	0
1.0×10^{-10}	9.81×10^{-11}	19.97	0.0284	2.00	132.7	0
1.0×10^{-11}	9.81×10^{-12}	22.82	0.0133	1.27	63.31	0
1.0×10^{-12}	9.81×10^{-13}	24.45	0.00617	0.855	33.07	0
1.0×10^{-13}	9.80×10^{-14}	25.30	0.00287	0.640	18.82	0
1.0×10^{-14}	9.80×10^{-15}	25.71	0.00133	0.535	1384.0	3.19×10^{-5}

Table IV. Numerical results for $C_c^\infty = 2.78 \times 10^{-4} \text{ mol/cm}^3$ and $C_a^\infty = 1.0 \times 10^{-8} \text{ mol/cm}^3$.

η (V)	$10^9 C_a^I$ (mol/cm ³)	C_c^I (mol/cm ³)	$\theta^{(0)}$	$10^7 V$ (cm/s)	ω_c (cm ⁻¹)	σ_i (s ⁻¹)
-0.1	9.97	2.63×10^{-4}	0.0303	0.395	4.22×10^2	0
-0.2	9.83	1.10×10^{-4}	0.127	4.29	7.57×10^2	0
-0.3	9.08	1.18×10^{-5}	0.275	6.79	3.73×10^3	0
-0.4	6.31	1.20×10^{-6}	0.403	7.06	2.00×10^4	0
-0.5	2.19	1.45×10^{-7}	0.480	7.09	4.57×10^5	0.283

spectively. Table IV summarizes the results at different overpotentials η for $C_a^\infty = 1.0 \times 10^{-8} \text{ mol/cm}^3$. The values of the critical wavenumbers ω_c and the imaginary part of the growth rate σ_i at the onset of instability are given. Also included are the unperturbed values of the catalyst concentration at the interface C_a^I , the copper concentration at the interface C_c^I , the dimensionless coverage of adsorbed catalyst $\theta^{(0)}$, and the interface velocity V .

From Table II, C_a^I is approximately 90% of C_a^∞ over seven orders of magnitude of catalyst concentration. Thus, only a small concentration gradient of catalyst exists in the electrolyte for the kinetically limited catalyst accumulation. As C_a^∞ decreases, the steady-state coverage of adsorbed catalyst $\theta^{(0)}$ also decreases. With less adsorbed catalyst, the interface velocity (*i.e.*, the copper deposition rate) decreases, and the copper concentration at the interface increases towards the bulk value. For the smaller values of C_a^∞ , the critical wavenumber corresponds to a complex mode, with a value of ω_c that tends toward a limiting value near 10^4 cm^{-1} as C_a^∞ decreases. For the larger values of C_a^∞ , the critical wavenumber ω_c corresponds to a real mode with ω_c increasing as C_a^∞ increases.

The dependence of the critical wavenumber on the catalyst concentration summarized in Table II is also plotted in Fig. 3 (additional points have been added for clarity). The greatest stabilization of the surface is for the lowest value of ω_c , which occurs at about 300 cm^{-1} for catalyst concentration $C_a^\infty \approx 10^{-10} \text{ mol/cm}^3$ for $\eta = -0.3 \text{ V}$. This optimum condition corresponds to the junction of the real and complex modes having $\sigma_r = 0$.

When the catalyst concentration falls to a value where the CEAC brightening mechanism no longer functions effectively, near C_a^∞

$= 10^{-11} \text{ mol/cm}^3$, destabilization is rapid. This sensitivity of ω_c to C_a^∞ for the complex modes arises from the near-independence of σ_r of these modes to wavenumber (see Fig. 1 and 2); because the σ_r curve for the complex mode is nearly horizontal, its intercept on the horizontal axis (*i.e.*, ω_c) is extremely sensitive to the vertical displacements of the curve associated with different values of C_a^∞ . The more gradual increase of ω_c at the higher concentrations C_a^∞ associated with the real modes derives in part from the destabilizing cupric ion gradient associated with the increasing deposition rate.

Numerical results for $\eta = -0.2 \text{ V}$ are given in Table III, and the corresponding critical wavenumbers are also plotted in Fig. 3. The critical wavenumbers are lower than those for $\eta = -0.3 \text{ V}$, indicating greater stability for any particular catalyst concentration C_a^∞ . This is consistent with what would be expected for the smaller, destabilizing concentration gradient of the cupric ion, indicated by the reduced cupric ion depletion at the interface for deposition at -0.2 V (Tables II and III). The rapid increase of ω_c occurs at concentration C_a^∞ approximately two orders of magnitude lower than for depositions at $\eta = -0.3 \text{ V}$ and, again, marks a transition from real to complex modes. The increased stability is due, in some part, to the smaller cupric ion gradient at $\eta = -0.2 \text{ V}$.

In terms of the stability criteria given in Eq. 50 and 51, the instability at $\omega < \omega_c$ for concentrations C_a^∞ with complex roots arises by violation of Eq. 50. For these lower concentrations C_a^∞ and associated coverages $\theta^{(0)}$, the right side of Eq. 50 is positive, and the mode is only stabilized by the surface tension term on the left side. For larger values of C_a^∞ , the right side of Eq. 50 is negative, making the criterion satisfied for all wavenumbers, and Eq. 51 therefore determines stability.

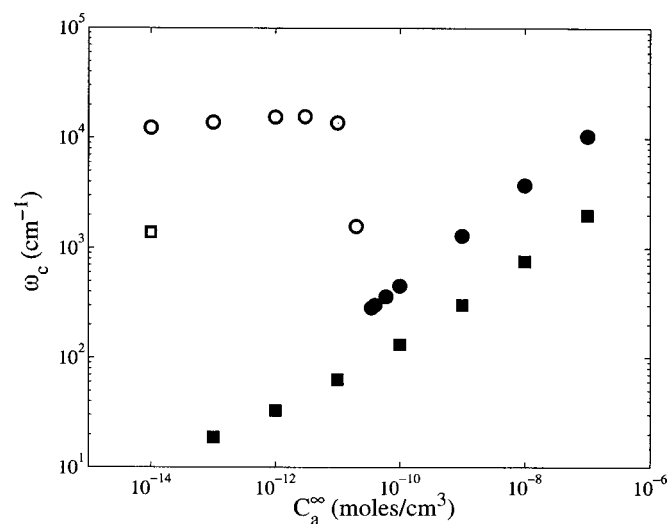


Figure 3. Critical wavenumber ω_c vs. C_a^∞ for $C_c^\infty = 2.78 \times 10^{-4} \text{ mol/cm}^3$. Closed symbols correspond to real modes, and open symbols correspond to complex modes (see Tables II and III). For $\eta = -0.3$ and -0.2 V , the data points are indicated by circles and squares, respectively. The system is stable for $\omega > \omega_c$.

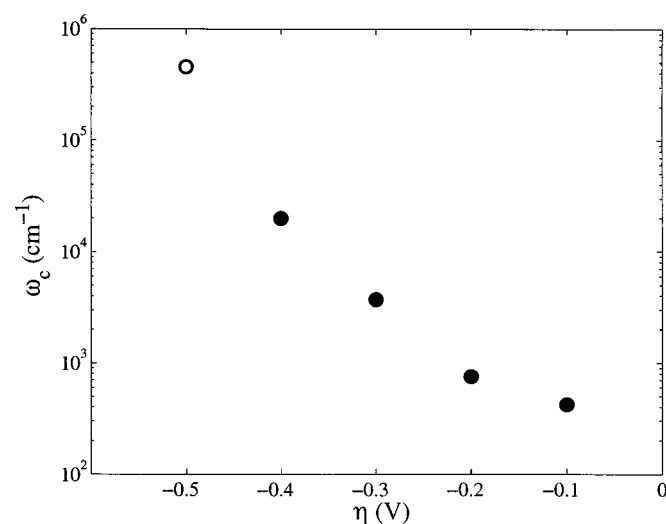


Figure 4. Critical wavenumber ω_c vs. η for $C_c^\infty = 2.78 \times 10^{-4} \text{ mol/cm}^3$ and $C_a^\infty = 1.0 \times 10^{-8} \text{ mol/cm}^3$. The open circle is a complex mode (see Table IV). The system is stable for $\omega > \omega_c$.

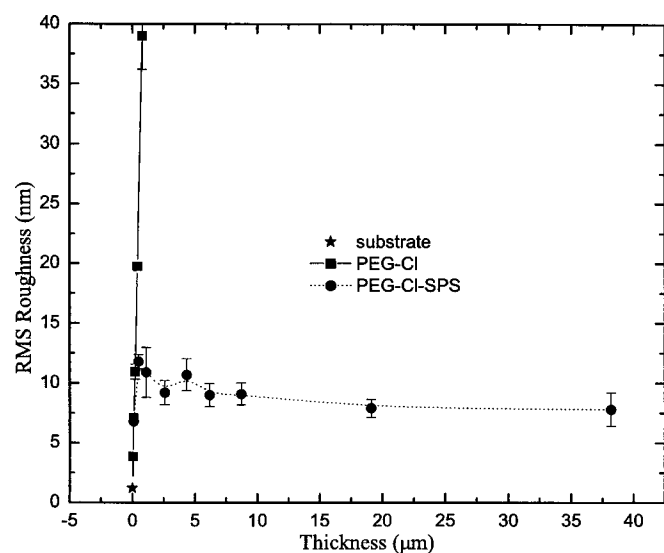


Figure 5. The measured rms roughness vs. deposit thickness with and without SPS in the electrolyte. Film thicknesses were determined by integrating the time-dependent deposition currents for each specimen using the known charge of the Cu^{2+} ions and the surface area of the deposits. Specimen thickness variation was obtained by changing deposition time alone.

Results for ω_c as a function of overpotential η for $C_a^\infty = 1.0 \times 10^{-8}$ mol/cm³ are given in Table IV and Fig. 4. As η varies from -0.1 to -0.5 V, the system becomes increasing unstable; for $\eta = -0.5$ V the critical wavenumber corresponds to a complex mode.

Experimental Results

Comparison to experimental observations of the surface roughness of deposits provides strong support for the proposed mechanism. Roughness measurements were made for deposits from electrolytes with and without catalyst. Films were grown at a fixed overpotential of -0.25 V for fixed times, rinsed in distilled water, and transferred to an atomic force microscope (AFM) for roughness measurements. For the purposes of this work, only the saturation roughness for each specimen (the scan-length independent value obtained for sufficiently large scans) is presented.

Both electrolytes contained 0.25 mol/L $\text{CuSO}_4 \cdot 5\text{H}_2\text{O}$ and 1.8 mol/L H_2SO_4 , 10^{-3} mol/L Cl^- , and 88.2×10^{-6} mol/L of 3400 molecular weight polyethylene glycol (PEG) additives; the latter two components suppress copper deposition. A concentration of 6×10^{-6} mol/L of the disulfide catalyst $\text{Na}_2 [\text{SO}_3(\text{CH}_2)_3\text{S}]_2$ was used for the catalyst containing electrolyte. The deposition rate and the kinetics for catalyst adsorption and consumption summarized in Table I and Eq. 5 and 6 as used in the modeling sections are representative of those obtained experimentally for this electrolyte-catalyst system.²⁵ Kinetics, aside from consumption, have also been published previously for a similar electrolyte-catalyst system.¹⁸⁻²¹

Figure 5 summarizes the thickness-dependent root-mean-square (rms) roughness of copper deposits made in the electrolytes. Because the modeling presented here is based on perturbations about steady-state deposition conditions, it is not expected to describe surface evolution during the approach to steady-state conditions, and thus the transient period of roughening in both electrolytes is not addressed here. More relevantly, after approximately 0.5 μm of deposition, the surface roughness of deposits from the electrolyte containing the SPS catalyst stabilizes and begins to attenuate slightly with further growth. This is consistent with the stabilization to very long wavelengths (very small ω_c) predicted by the model for this overpotential and catalyst concentration (Fig. 3). In contrast, the

deposits from the electrolyte with no catalyst continue to roughen, with rms roughness reaching 70 nm rms at 300 s.

It is worth noting that, at -0.25 V overpotential, the steady-state metal deposition rate in the catalyst-containing electrolyte is approximately four times faster than that in the catalyst-free electrolyte. The corresponding depletion of cupric ion at the growth surface is approximately 20% from the bulk concentration for the catalyst-free electrolyte vs. approximately 85% for the catalyst-containing electrolyte; these values are based on steady-state currents for deposition under the given conditions (not shown). Thus, the deposits from the catalyst-containing electrolyte are smoother in spite of having been grown in a steeper metal-ion concentration gradient in the electrolyte. A more thorough comparison of modeling and experimental results will be published separately.

Discussion

The long-term saturation, and attenuation, of roughness observed experimentally is as predicted. These results suggest that the CEAC mechanism originally proposed to describe superconformal filling of vias and trenches can also function as a mechanism for creating bright, planar deposits.

These results clearly indicate a potential mechanism by which catalyst containing electrolytes can maintain planar surfaces during deposition, yielding bright deposits (subject to instabilities at larger length scales that arise from the finite boundary layer thickness). Interestingly, there is predicted to be no stabilization absent competition between accumulation and consumption establishing the coverage. Thus no stabilization is predicted for a system where an initial coverage of catalyst is achieved prior to deposition with negligible accumulation or consumption during the metal deposition process. Therefore, this result, while explaining how catalyst-containing electrolytes yield bright deposits, does not explain why reduced roughness is also observed in experiments where catalyst is adsorbed on surfaces prior to metal deposition. Such an explanation might be obtained by going to higher order in the stability analysis to seek a stable state with a finite, nonzero perturbation amplitude.

It is presumptuous to extract much more than the largest length scale for which a perturbation is stable from a first-order perturbation analysis. Nonetheless, it is worth noting that complex exponents, with a negative real component, mean that some perturbations will decay in an oscillatory manner. In such a case the deposit thickness at a particular location will exhibit oscillatory deviations from the average growth surface, with successively smaller maximum positive and negative deviations with time. It was noted at the start of this work that the CEAC mechanism responsible for the brightening presented here also causes the bottom-to-top filling of submicrometer features. Such filling is typically followed by development of an overflow bump that subsequently decays back to the planar growth front.^{18-20,23} This behavior is analogous to the damped oscillatory behavior described above.

Acknowledgments

The authors are grateful for helpful discussions with K. F. Gurski and J. E. Guyer. We acknowledge partial support of this work from the NASA Physical Sciences Division.

National Institute of Standards and Technology assisted in meeting the publication costs of this article.

References

- W. W. Mullins and R. F. Sekerka, *J. Appl. Phys.*, **35**, 444 (1964).
- S. R. Coriell and G. B. McFadden, in *Handbook of Crystal Growth*, Vol. 1B, p. 785, D. T. J. Hurle, Editor, Elsevier, Amsterdam (1993).
- R. Aogaki, K. Kitazawa, Y. Kose, and K. Fueki, *Electrochim. Acta*, **25**, 965 (1980).
- R. Aogaki and T. Makino, *Electrochim. Acta*, **26**, 1509 (1981).
- R. Aogaki, *J. Electrochem. Soc.*, **129**, 2442 (1982).
- R. Aogaki and T. Makino, *J. Electrochem. Soc.*, **131**, 40 (1984).
- R. Aogaki and T. Makino, *J. Chem. Phys.*, **81**, 2154 (1984).
- R. Aogaki and T. Makino, *J. Chem. Phys.*, **81**, 2164 (1984).
- D. P. Barkey, R. H. Muller, and C. W. Tobias, *J. Electrochem. Soc.*, **136**, 2199 (1989).

10. D. P. Barkey, R. H. Muller, and C. W. Tobias, *J. Electrochem. Soc.*, **136**, 2207 (1989).
11. C.-P. Chen and J. Jorne, *J. Electrochem. Soc.*, **138**, 3305 (1991).
12. C. H. J. Van Den Brekel and A. K. Jensen, *J. Cryst. Growth*, **43**, 364 (1978).
13. C. H. J. Van Den Brekel and A. K. Jensen, *J. Cryst. Growth*, **43**, 371 (1978).
14. C. Madore, M. Matlosz, and D. Landolt, *J. Electrochem. Soc.*, **143**, 3927 (1996), and numerous references therein.
15. C. Madore and D. Landolt, *J. Electrochem. Soc.*, **143**, 3936 (1996).
16. D. Roha and U. Landau, *J. Electrochem. Soc.*, **137**, 824 (1990).
17. A. C. West, *J. Electrochem. Soc.*, **147**, 227 (2000).
18. T. P. Moffat, D. Wheeler, W. H. Huber, and D. Josell, *Electrochem. Solid-State Lett.*, **4**, C26 (2001).
19. D. Josell, D. Wheeler, W. H. Huber, and T. P. Moffat, *Phys. Rev. Lett.*, **87**, article no. 016102 (2001).
20. D. Wheeler, D. Josell, and T. P. Moffat, *J. Electrochem. Soc.*, **150**, C302 (2003).
21. D. Josell, D. Wheeler, W. H. Huber, J. E. Bonevich, and T. P. Moffat, *J. Electrochem. Soc.*, **148**, C767 (2001).
22. D. Josell, D. Wheeler, and T. P. Moffat, *Electrochem. Solid-State Lett.*, **5**, C49 (2002).
23. D. Josell, D. Wheeler, and T. P. Moffat, *Electrochem. Solid-State Lett.*, **5**, C44 (2002).
24. F. R. Gantmacher, *The Theory of Matrices*, Vol. II, Chelsea, New York (1959).
25. T. P. Moffat, Unpublished results.